Supplementary Materials
Maximal quantum interaction between free electrons and photons

Zetao Xie,[1,*] Zeling Chen,[1,*] Hao Li,[2] Qinghui Yan,[3,4] Hongsheng Chen,[3] Xiao Lin,[3] Ido Kaminer,[4] Owen D. Miller,[2,†] and Yi Yang[1,‡]

[1] *Department of Physics and HK Institute of Quantum Science and Technology, The University of Hong Kong, Pokfulam, Hong Kong, China*

[2] *Department of Applied Physics & Energy Sciences Institute, Yale University, New Haven, CT 06520, USA*

[3] *Interdisciplinary Center for Quantum Information, State Key Laboratory of Modern Optical Instrumentation, College of Information Science and Electronic Engineering, Zhejiang University, Hangzhou 310027, China*

[4] *Solid State Institute and Faculty of Electrical and Computer Engineering, Technion – Israel Institute of Technology, 32000 Haifa, Israel*

CONTENTS

S1. QUANTUM INTERACTION STRENGTH BETWEEN FREE ELECTRONS AND PHOTONS

The quantum interaction strength g_{Q} is a dimensionless complex parameter accounting for electron-photon coupling strength and phase. $|g_{\mathrm{Q}}|^2$ for an electromagnetic single mode can be calculated by integrating the energy loss probability across the spectrum based on the derivation of quantum electrodynamic [S1; S2; S3; S4]. In this section, we outline the derivation by following key steps in Ref. [S1]. Considering the free electrons do not traverse the material (i.e., a gauge with zero scalar potential), the formal solution of the vector potential operator $\hat{\mathbf{A}}$ in the quantized three-dimensional Maxwell equation is given as [S1; S5; S6]

$$\hat{\mathbf{A}}(\mathbf{r},\omega) = -\frac{1}{\epsilon_0}\int \mathrm{d}^3\mathbf{r}\mathbb{G}(\mathbf{r},\mathbf{r}',\omega)\cdot\hat{\mathbf{j}}^{\mathrm{noise}}(\mathbf{r}',\omega), \tag{S1}$$

where $\mathbb{G}(\mathbf{r},\mathbf{r}',\omega)$ is the classic electromagnetic Green tensor, which satisfies the relation:

$$\boldsymbol{\nabla}\times\boldsymbol{\nabla}\times\mathbb{G}(\mathbf{r},\mathbf{r}',\omega) - \frac{\omega^2}{c^2}\epsilon(\mathbf{r},\omega)\mathbb{G}(\mathbf{r},\mathbf{r}',\omega) = -\frac{1}{c^2}\delta(\mathbf{r}-\mathbf{r}'). \tag{S2}$$

$\hat{\mathbf{j}}^{\mathrm{noise}}$ is a noise current operator which represents the dissipation when the electromagnetic field interacts with the material

$$\hat{\mathbf{j}}^{\mathrm{noise}}(\mathbf{r},\omega) = \omega\sqrt{4\pi\epsilon_0\hbar\mathrm{Im}\left\{\epsilon(\mathbf{r},\omega)\right\}}\mathbf{f}(\mathbf{r},\omega), \tag{S3}$$

where $\mathbf{f}(\mathbf{r},\omega)$ is bosonic operator, $\epsilon(\mathbf{r},\omega)$ is the relative permittivity, and the evolution is governed by the radiation Hamiltonian [S5]:

$$\hat{H}_{\mathrm{rad}} = \int \mathrm{d}^3\mathbf{r}\int_0^\infty \mathrm{d}\omega\hbar\omega\mathbf{f}^\dagger(\mathbf{r},\omega)\cdot\mathbf{f}(\mathbf{r},\omega). \tag{S4}$$

Assuming an electron beam with narrow momentum distribution around its wave vector $\mathbf{k}_0$, and the entangled photon energy is smaller than the electron relativistic energy $\mathcal{E}_0$, the free electron Hamiltonian $\hat{H}_{\rm el}$ is [S7]

$$\hat{H}_{\rm el} = \sum_{\mathbf{k}} \left[\mathcal{E}_0 + \hbar \mathbf{v}\cdot(\mathbf{k}-\mathbf{k}_0)\right] \hat{c}^{\dagger}_{\mathbf{k}} \hat{c}_{\mathbf{k}}, \tag{S5}$$

where $\mathbf{v} = \hbar c^2 \mathbf{k}_0 / E_0$ is the central electron velocity, $\hat{c}^{\dagger}_{\mathbf{k}}$ ($\hat{c}_{\mathbf{k}}$) is anticommuting creation (annihilation) operator of an electron with momentum $\hbar\mathbf{k}$. The interaction between the electromagnetic field and the electron can be described by the interaction Hamiltonian $\hat{H}_{\rm int}$ in the interaction picture [S1; S6]:

$$\hat{H}_{\rm int}(t) = -\int \mathrm{d}^3\mathbf{r} \hat{\mathbf{A}}(\mathbf{r},t)\cdot\hat{\mathbf{j}}^{\rm el}(\mathbf{r},t), \tag{S6}$$

where $\hat{\mathbf{j}}^{\rm el}(\mathbf{r},t) = (-e\mathbf{v}/V)\sum_{\mathbf{k},\mathbf{q}} \mathrm{e}^{\mathrm{i}\mathbf{q}\cdot(\mathbf{r}-\mathbf{v}t)} \hat{c}^{\dagger}_{\mathbf{k}} \hat{c}_{\mathbf{k}+\mathbf{q}}$ is the electron current operator, $\hat{\mathbf{A}}(\mathbf{r},t) = \int_0^{\infty} \frac{\mathrm{d}\omega}{2\pi} \hat{\mathbf{A}}(\mathbf{r},\omega)\mathrm{e}^{-\mathrm{i}\omega t} +$ h.c., $\mathbf{q}$ is the exchanged wave vector, and V is the volume of the quantization box. The scattering operator governing the system's evolution from $t = -\infty$ to $t = \infty$ can be described as [S1]:

$$\hat{S}_{\rm int}(-\infty,\infty) = \mathrm{e}^{\mathrm{i}\hat{\chi}(-\infty,\infty)} \mathrm{e}^{-\frac{\mathrm{i}}{\hbar}\int_{-\infty}^{\infty}\mathrm{d}t' \hat{H}_{\rm int}(t')} = \mathrm{e}^{\mathrm{i}\hat{\chi}(-\infty,\infty)} \hat{U}(-\infty,\infty). \tag{S7}$$

Here

$$\hat{U}(-\infty,\infty) = \exp\left\{\left[\frac{-\mathrm{i}e}{2\pi\hbar V^{2/3}} \sum_{\mathbf{k},\mathbf{q}_{\perp}} \int_0^{\infty} \mathrm{d}\omega \int \mathrm{d}^3\mathbf{r} \mathrm{e}^{\mathrm{i}\mathbf{q}_{\perp}\cdot\mathbf{R}} \mathrm{e}^{-\mathrm{i}\omega z/v} \hat{\mathbf{A}}_z(\mathbf{r},\omega) \hat{c}^{\dagger}_{\mathbf{k}} \hat{c}_{\mathbf{k}+\mathbf{q}_{\perp}-(\omega/v)\hat{\mathbf{z}}}\right] - \text{h.c.}\right\}, \tag{S8}$$

and $\hat{\chi}$ is the phase operator that only affects the electron degrees of freedom. For an electron at $\mathbf{R} = \mathbf{R}_0$, the wave function can be separated into longitudinal and transverse components, by replacing the exponent operator in $\hat{U}$ with its average over a transverse electron state, Eq. (S8) can be further simplified as:

$$\hat{U}(-\infty,\infty) = \exp\left[\int \mathrm{d}\omega \left(g_{\mathrm{Q},\omega} \hat{b}^{\dagger}_{\omega} \hat{a}_{\omega} - g^{*}_{\mathrm{Q},\omega} \hat{b}_{\omega} \hat{a}^{\dagger}_{\omega}\right)\right], \tag{S9}$$

with

$$\hat{a}_{\omega} = -\frac{\mathrm{i}e}{2\pi\hbar g_{\mathrm{Q},\omega}} \int_{-\infty}^{\infty} \mathrm{d}z \mathrm{e}^{-\mathrm{i}\omega z/v} \hat{\mathbf{A}}_z(\mathbf{R}_0, z, \omega), \tag{S10}$$

$$\hat{b}_{\omega} = \sum_{k_z} \hat{c}^{\dagger}_{k_z} \hat{c}_{k_z+\omega/v}, \tag{S11}$$

where $g_{\mathrm{Q},\omega}$ is the quantum interaction strength at a given frequency ω, which is the square root of the EELS probability [S8]:

$$\begin{aligned} |g_{\mathrm{Q},\omega}|^2 &= \Gamma(\mathbf{R}_0,\omega) \\ &= \frac{e^2}{\pi\epsilon_0\hbar} \int_{-\infty}^{\infty} \mathrm{d}z \int_{-\infty}^{\infty} \mathrm{d}z' \cos\left[\frac{\omega(z-z')}{v}\right] \mathrm{Im}\left\{-G^{\rm ind}_{zz}(\mathbf{R}_0, z, \mathbf{R}_0, z', \omega)\right\}, \end{aligned} \tag{S12}$$

where $G^{\rm ind}_{zz} = \hat{\mathbf{z}}\cdot\mathbb{G}^{\rm ind}\cdot\hat{\mathbf{z}}$ represents the induced Green tensor projected along z axis. Therefore, the quantum interaction strength of a single mode is calculated by $|g_{\mathrm{Q}}|^2 = \int |g_{\mathrm{Q},\omega}|^2 \,\mathrm{d}\omega = \int \Gamma(\mathbf{R}_0,\omega)\,\mathrm{d}\omega$.

S2. THE SCATTERING $\mathbb{T}$ MATRIX

The scattering $\mathbb{T}$ matrix ($\mathbb{T}$ operator) is a mathematical representation used in scattering theory to elucidate the interaction of electromagnetic waves with an object. The recently developed frameworks show that the $\mathbb{T}$ matrix provides a powerful tool for understanding the scattering process and has been effectively applied to the analysis of plane-wave scattering and radiative heat transfer [S9; S10; S11]. In this section, we briefly summarize the fundamental properties of the $\mathbb{T}$ matrix, covering its definition, Kramers–Kronig (KK) relations, sum rules, and constraints.

A. Definition of the $\mathbb{T}$ matrix

For a scattering problem where the total field $\mathbf{E}_{\text{tot}}(\mathbf{r})$ is the sum of a known incident field $\mathbf{E}_{\text{inc}}(\mathbf{r})$ and scattered field $\mathbf{E}_{\text{scat}}(\mathbf{r})$, $\mathbf{E}_{\text{tot}}(\mathbf{r}) = \mathbf{E}_{\text{inc}}(\mathbf{r}) + \mathbf{E}_{\text{scat}}(\mathbf{r})$. The scattered field $\mathbf{E}_{\text{scat}}(\mathbf{r})$ is determined by the convolution of the free-space Green Function $\mathbb{G}_0$ with the polarization field representing the response of the scattering object to the incident field, $\mathbf{E}_{\text{scat}}(\mathbf{r}) = \int_V \mathbb{G}_0(\mathbf{r}, \mathbf{r}')\mathbf{P}(\mathbf{r}')\mathrm{d}\mathbf{r}'$. Consider the scatter with material electric susceptibility $\chi(\mathbf{r})$, the total field $\mathbf{E}_{\text{tot}}(\mathbf{r})$ is equal to the induced polarization field $\mathbf{P}(\mathbf{r})$ divided by the susceptibility within the scatter. Consequently, the incident field $\mathbf{E}_{\text{inc}}(\mathbf{r})$ can be rewritten in terms of the polarization field

$$\mathbf{E}_{\text{inc}}(\mathbf{r}) = \mathbf{E}_{\text{tot}}(\mathbf{r}) - \mathbf{E}_{\text{scat}}(\mathbf{r}) = \frac{\mathbf{P}(\mathbf{r})}{\chi(\mathbf{r})} - \int_V \mathbb{G}_0(\mathbf{r}, \mathbf{r}')\mathbf{P}(\mathbf{r}')\mathrm{d}\mathbf{r}'. \tag{S13}$$

Here, the vacuum permittivity ϵ_0 is implicitly defined as unity, and ϵ_0 will be restored in the limits of g_{Q}.

Assuming any arbitrarily spatial high-accuracy discretization, wherein $\mathbf{P}(\mathbf{r})$ is represented as a vector $\mathbf{p}$, the incident fields $\mathbf{E}_{\text{inc}}(\mathbf{r})$ becomes a vector $\mathbf{e}_{\text{inc}}$, we can rewrite Eq. (S13) in vector notation then invert the matrices in square brackets

$$\mathbf{p} = \left[\chi^{-1} - \mathbb{G}_0\right]^{-1} \mathbf{e}_{\text{inc}} = \mathbb{T}\mathbf{e}_{\text{inc}}, \tag{S14}$$

and $\mathbb{T}$ is defined as

$$\mathbb{T} = \left[\chi^{-1} - \mathbb{G}_0\right]^{-1}. \tag{S15}$$

Here, the $\mathbb{T}$ matrix is a causal linear electromagnetic scattering function that relates the incident field to the polarization field [S11; S12].

B. $\mathbb{T}$-matrix Kramers–Kronig relation

In the time domain, the $\mathbb{T}$ matrix is defined to connect the incident field to the polarization field, analogous to the convolutional time-domain relationship of material susceptibility [S13],

$$\mathbf{p}(t) = \int \mathbb{T}(t - t')\mathbf{e}_{\text{inc}}(t')\,\mathrm{d}t'. \tag{S16}$$

The above definition of $\mathbb{T}$ encodes the causality similar to material susceptibilities, stipulating that the polarization field cannot arise before the incident electric field reaches. Thus, $\mathbb{T}$ is identically zero at all preceding times before the original time t', that is, $\mathbb{T}(t < t') = 0$. By taking the Fourier transform of the time-domain $\mathbb{T}$ matrix, one can obtain the frequency-domain $\mathbb{T}$ matrix

$$\mathbb{T}(\omega) = \int_{-\infty}^{\infty} \mathbb{T}(t)\mathrm{e}^{\mathrm{i}\omega t}\,\mathrm{d}t = \int_{0}^{\infty} \mathbb{T}(t)\mathrm{e}^{\mathrm{i}\omega t}\,\mathrm{d}t. \tag{S17}$$

Here, the causality condition sets the interval of integral from 0 to ∞. $\mathbb{T}$ matrix is complex analytic in the upper half of the complex-frequency plane [S11]. Thus, we can use Cauchy's integral theorem to the following closed-contour integral

$$\int_C \frac{\mathbb{T}(\omega')}{\omega' - \omega}\,\mathrm{d}\omega' = 0. \tag{S18}$$

The closed contour C can be decomposed into three components: (1) the integral along the real axis from negative infinity to infinity but skipping a simple pole at ω; (2) the integral of a large semicircular arc in the upper half-plane, which goes to zero for infinite frequency; (3) the integral of a small semicircular

arc rotating clockwise around ω, which is equal to half of the Cauchy residue term with a negative sign, -i$\pi\mathbb{T}(\omega)$. By removing (2) and setting (1) equal to the negation of (3), we have

$$\mathrm{i}\pi\mathbb{T}(\omega) = \int_{-\infty}^{\infty} \frac{\mathbb{T}(\omega')}{\omega' - \omega}\,\mathrm{d}\omega'. \tag{S19}$$

Next, we substitute $\mathbb{T}(\omega) = \mathrm{Re}\mathbb{T}(\omega) + \mathrm{iIm}\mathbb{T}(\omega)$ into Eq. (S19) and equate the real parts and imaginary parts of both sides, respectively

$$\mathrm{Re}\mathbb{T}(\omega) = \frac{1}{\pi}\int_{-\infty}^{\infty} \frac{\mathrm{Im}\mathbb{T}(\omega')}{\omega' - \omega}\,\mathrm{d}\omega', \tag{S20}$$

$$\mathrm{Im}\mathbb{T}(\omega) = -\frac{1}{\pi}\int_{-\infty}^{\infty} \frac{\mathrm{Re}\mathbb{T}(\omega')}{\omega' - \omega}\,\mathrm{d}\omega'. \tag{S21}$$

The realness of the time-domain electric field ensure that $\mathbb{T}(-\omega^*) = \mathbb{T}^*(\omega)$ where the complex conjugate applies to each matrix element. For reciprocal systems, the condition can be further formulated as $\mathbb{T}(-\omega^*) = \mathbb{T}^\dagger(\omega)$, whose real and imaginary parts satisfy

$$\mathrm{Re}\mathbb{T}(-\omega) = \mathrm{Re}\mathbb{T}(\omega), \tag{S22}$$

$$\mathrm{Im}\mathbb{T}(-\omega) = -\mathrm{Im}\mathbb{T}(\omega), \tag{S23}$$

along the real frequency axis. Hence, Eqs. (S20) and (S21) can be rewritten as

$$\begin{aligned}\mathrm{Re}\mathbb{T}(\omega) &= \frac{1}{\pi}\int_{-\infty}^{\infty} \frac{(\omega' + \omega)\,\mathrm{Im}\mathbb{T}(\omega')}{\omega'^2 - \omega^2}\,\mathrm{d}\omega' \\ &= \frac{1}{\pi}\int_{-\infty}^{\infty} \frac{\omega'\mathrm{Im}\mathbb{T}(\omega')}{\omega'^2 - \omega^2}\,\mathrm{d}\omega' \\ &= \frac{2}{\pi}\int_{0}^{\infty} \frac{\omega'\mathrm{Im}\mathbb{T}(\omega')}{\omega'^2 - \omega^2}\,\mathrm{d}\omega',\end{aligned} \tag{S24}$$

$$\begin{aligned}\mathrm{Im}\mathbb{T}(\omega) &= -\frac{1}{\pi}\int_{-\infty}^{\infty} \frac{(\omega' + \omega)\,\mathrm{Re}\mathbb{T}(\omega')}{\omega'^2 - \omega^2}\,\mathrm{d}\omega' \\ &= -\frac{1}{\pi}\int_{-\infty}^{\infty} \frac{\omega\mathrm{Re}\mathbb{T}(\omega')}{\omega'^2 - \omega^2}\,\mathrm{d}\omega' \\ &= -\frac{2\omega}{\pi}\int_{0}^{\infty} \frac{\mathrm{Re}\mathbb{T}(\omega')}{\omega'^2 - \omega^2}\,\mathrm{d}\omega',\end{aligned} \tag{S25}$$

which are the Kramers–Kronig (KK) relations for the $\mathbb{T}$ matrix.

C. Sum rules

KK relations of the $\mathbb{T}$ matrix derived above are the foundations of the sum rules in this section. To obtain the sum rules, we consider two special frequency poles at the right-hand side of Eq. (S24): infinite frequency and zero frequency.

At infinite frequency, materials become transparent with susceptibilities scale as $\chi(\omega) \to -\omega_\mathrm{p}^2/\omega^2$ (ω_p is a constant proportional to the total electron density of the material and is known as the plasma frequency for metals) [S14]. Thus, the polarization field can be approximated as $\mathbf{P} = \chi\mathbf{E}_\mathrm{tot} \simeq \chi\mathbf{E}_\mathrm{inc} \simeq \left(-\omega_\mathrm{p}^2/\omega^2\right)\mathbf{E}_\mathrm{inc}$ based on the first Born approximation, indicating that the $\mathbb{T}$ matrix asymptotically approaches $-\omega_\mathrm{p}^2/\omega^2\mathbb{I}_V$ ($\mathbb{I}_V$ is the identity matrix of the scatterer with volume V). By inserting the infinite-frequency limit into Eq. (S24), we have the infinite-frequency sum rule as follows

$$\mathrm{Re}\mathbb{T}(\omega \to \infty) = \frac{2}{\pi}\int_{0}^{\infty} \frac{\omega'\mathrm{Im}\mathbb{T}(\omega')}{\omega'^2 - \omega^2}\,\mathrm{d}\omega' = -\frac{\omega_\mathrm{p}^2}{\omega^2}\mathbb{I}_V, \tag{S26}$$

$$\int_0^\infty \omega' \mathrm{Im}\mathbb{T}(\omega')\,\mathrm{d}\omega' = \frac{\pi\omega_\mathrm{p}^2}{2}\mathbb{I}_V. \tag{S27}$$

$\omega'\mathrm{Im}\mathbb{T}(\omega')$ can be written in a basis as the sum of the product of the delta function and frequency-independent matrix $\mathbb{T}_i$. Thus, the discrete representation is given by

$$\omega'\mathrm{Im}\mathbb{T}(\omega') = \frac{\pi\omega_\mathrm{p}^2}{2}\sum_{i=1}^{\infty}\mathbb{T}_i\delta\left(\omega'-\omega_i\right), \tag{S28}$$

where all matrices $\mathbb{T}_i$ are positive semidefinite due to passivity and $\sum_{i=1}^{\infty}\mathbb{T}_i = \mathbb{I}_V$ because of the sum rule.

For another pole at zero frequency, we can write $\mathrm{Re}\mathbb{T}(\omega=0)=\boldsymbol{\tau}$, where $\boldsymbol{\tau}$ is the generalized electrostatic matrix. Inserting the expression into the KK relation Eq. (S24) yields a zero-frequency sum rule for arbitrary scatterers

$$\mathrm{Re}\mathbb{T}(\omega=0) = \frac{2}{\pi}\int_0^\infty \frac{\mathrm{Im}\mathbb{T}(\omega')}{\omega'}\,\mathrm{d}\omega' = \boldsymbol{\tau}. \tag{S29}$$

Considering a designable region D encloses an arbitrary scatterer V, the electrostatic matrix $\boldsymbol{\tau}$ of the designable region becomes a scalar function of the electrostatic coefficient τ multiplied by the identity matrix $\mathbb{I}_D$. Thus, all possible canonical geometries satisfy:

$$\frac{2}{\pi}\int_0^\infty \frac{\mathrm{Im}\mathbb{T}(\omega')}{\omega'}\,\mathrm{d}\omega' \le \tau\mathbb{I}_D, \tag{S30}$$

or, in discrete representation

$$\omega'\mathrm{Im}\mathbb{T}(\omega') \le \frac{\pi\tau}{2}\sum_{i=1}^{\infty}\omega'^2\mathbb{T}_i\delta\left(\omega'-\omega_i\right), \tag{S31}$$

where $\omega'^2\delta\left(\omega'-\omega_i\right) = \omega_i^2\delta\left(\omega'-\omega_i\right)$. Similarly, we have the conditions that $\mathbb{T}_i \ge 0$ and a sum-rule constraint $\sum_{i=1}^{\infty}\mathbb{T}_i = \mathbb{I}_V \le \mathbb{I}_D$.

We apply the zero-frequency sum rule instead of the infinite-frequency one Eq. (S28) in deriving the upper limit to g_Q because the former can generally provide a tighter bound for most of the frequency regime covered in this work; nevertheless, there may exist materials with low ω_p, for which a tighter bound can be obtained with Eq. (S28).

$\mathbb{T}$ matrix can be faithfully represented by a sum of lossless Drude–Lorentz oscillators, we insert Eq. (S31) into the KK-relations Eq. (S24), and then isolate the real and imaginary parts of $\mathbb{T}(\omega)$:

$$\begin{aligned}
\mathbb{T}(\omega) &= \mathrm{Re}\mathbb{T}(\omega) + \mathrm{i}\mathrm{Im}\mathbb{T}(\omega)\\
&\le \tau\sum_{i=1}^{\infty}\frac{\omega_i^2\mathbb{T}_i}{\omega_i^2-\omega^2} + \mathrm{i}\frac{\pi\tau}{2}\sum_{i=1}^{\infty}\omega_i\mathbb{T}_i\delta\left(\omega-\omega_i\right)\\
&= \tau\sum_{i=1}^{\infty}\left[\frac{\omega_i^2\mathbb{T}_i}{\omega_i^2-\omega^2} + \mathrm{i}\pi\omega_i^2\mathbb{T}_i\delta\left(\omega_i^2-\omega^2\right)\right]\\
&= \lim_{\gamma_\mathbb{T}\to 0}\sum_{i=1}^{\infty}\frac{\tau\omega_i^2\mathbb{T}_i}{\omega_i^2-\omega^2-\mathrm{i}\gamma_\mathbb{T}\omega},
\end{aligned} \tag{S32}$$

where we use the domain monotonicity of polarizability [S15] to enclose arbitrary-shaped scatterers with canonical structures in the inequality second line. We also use the fact that $\delta\left(\omega_i-\omega\right) = 2\omega\delta\left(\omega_i^2-\omega^2\right)$ from the second to the third line, and $\lim_{\gamma_\mathbb{T}\to 0}\frac{1}{x+\mathrm{i}\gamma} = \frac{1}{x} - \mathrm{i}\pi\delta(x)$ from the third to last line. This oscillator representation indicates that $\mathbb{T}$ matrix can be decomposed into a set of lossless Drude–Lorentz oscillators with degrees of freedom $\mathbb{T}_i$. The damping term $\gamma_\mathbb{T}$ can be finite or approach zero, indicating that the framework can handle both resonances (finite loss; in the complex upper half-plane) and guided modes (zero loss; on the real axis of the complex frequency plane).

D. Electrostatic coefficient

The zero frequency sum rule of $\mathbb{T}$ matrix indicates the electrostatic $\mathbb{T}_{0,V}$ is proportional to a dimensionless electrostatic coefficient τ that permits analytical treatment for canonical geometries. Here we first show the derivation of this coefficient for a half-space and a concentric cylinder, which are related to the validation cases discussed in the main text.

The electrostatic coefficient τ for canonical structures can be derived using the image charge method. Consider a planar interface that separates one semi-infinite dielectric with electrostatic relative permittivity ϵ_1 for $z > 0$ from another semi-infinite dielectric ϵ_2 for $z < 0$, a charged wire q charge per unit length is positioned at a distance d above the interface. In electrostatics, the image charge $q' = -\frac{\epsilon_2-\epsilon_1}{\epsilon_2+\epsilon_1}q$ is introduced for $z < 0$, and $q'' = \frac{2\epsilon_2}{\epsilon_2+\epsilon_1}q$ represents another image charge at the position of the charged wire [S16]. The incident field and total field at $z < 0$ can be written as $\mathbf{E}_{\text{inc}} = \frac{1}{2\pi\epsilon_1}\frac{q}{r}\mathbf{r}$ and $\mathbf{E}_{\text{tot}} = \frac{1}{2\pi\epsilon_2}\frac{q''}{r}\mathbf{r}$, respectively. Thus, the induced polarization field for $z < 0$ is given by

$$\mathbf{P}(z < 0) = \chi_2\mathbf{E}_{\text{tot}} = (\epsilon_2 - 1)\frac{\epsilon_1}{\epsilon_2}\frac{2\epsilon_2}{\epsilon_2 + \epsilon_1}\mathbf{E}_{\text{inc}} = 2\epsilon_1\frac{\epsilon_2 - 1}{\epsilon_2 + \epsilon_1}\mathbf{E}_{\text{inc}}, \tag{S33}$$

where the electrostatic coefficient is defined as $\tau = 2\epsilon_1\frac{\epsilon_2-1}{\epsilon_2+\epsilon_1}$. When the charged wire is in a vacuum (i.e. $\epsilon_1 = 1$), the electrostatic coefficient τ simplifies to $2\frac{\epsilon_2-1}{\epsilon_2+1}$, where ϵ_2 is the dielectric constant of the material at $z < 0$.

We next apply Gauss's law to find the electrostatic coefficient τ of a concentric cylinder. A charged wire q is located at the center of an infinitely long concentric cylinder made of a core of radius d and an infinitely thick shell. The electrostatic relative permittivity of the core and the shell are ϵ_1 and ϵ_2, respectively. The incident field and total field in the shell can be written as $\mathbf{E}_{\text{inc}} = \frac{1}{2\pi\epsilon_1}\frac{q}{r}\mathbf{r}$ and $\mathbf{E}_{\text{tot}} = \frac{1}{2\pi\epsilon_2}\frac{q}{r}\mathbf{r}$ by considering a cylindrical surface at $r > d$. We obtain the induced polarization field for $r > d$ as

$$\mathbf{P}(r > d) = \epsilon_1\frac{\epsilon_2 - 1}{\epsilon_2}\mathbf{E}_{\text{inc}}. \tag{S34}$$

Thus, the electrostatic coefficient is $\tau = \epsilon_1\frac{\epsilon_2-1}{\epsilon_2}$, which can be simplified to $\tau = \frac{\epsilon_2-1}{\epsilon_2}$ when the charged wire is in a vacuum.

The two examples above both deal with extended structures with continuous translational invariance along the electron velocity direction. We next show the electrostatic coefficient τ can be similarly obtained for isolated structures like a sphere.

For a charged wire q is located in medium ϵ_1 a distance $d + a$ from the center of a sphere ϵ_2 of radius a, an image charge q_l'' is introduced outside the sphere. The image charge is given by $q_l'' = \frac{\epsilon_2(2l+1)}{l(\epsilon_1+\epsilon_2)+\epsilon_1}q$, where l is the order of associated Legendre polynomials [S16]. Accordingly, the incident field and total field of the charged wire can be written as $\mathbf{E}_{\text{inc}} = \frac{1}{2\pi\epsilon_1}\frac{q}{r}\mathbf{r}$ and $\mathbf{E}_{\text{tot}} = \frac{1}{2\pi\epsilon_2}\frac{q_l''}{r}\mathbf{r}$, respectively, and the induced polarization field is:

$$\mathbf{P}_l = (\epsilon_2 - 1)\epsilon_1\frac{2l + 1}{l(\epsilon_1 + \epsilon_2) + \epsilon_1}\mathbf{E}_{\text{inc}}, \tag{S35}$$

in which the electrostatic coefficient is given as $\tau_l = (\epsilon_2 - 1)\epsilon_1\frac{2l+1}{l(\epsilon_1+\epsilon_2)+\epsilon_1}$ and reduced to $\tau_l = (\epsilon_2 - 1)\frac{2l+1}{l(\epsilon_2+1)+1}$ when the charged wire is in free-space.

The electrostatic coefficient τ is finite and bounded. For covalent and ionic materials, the dielectric constant is described by $\epsilon(0) = 1 + (4\pi\hbar n_{\text{v}}e^2)/m_{\text{e}}E_{\text{g}}^2$ where m_{e} is the electron mass, E_{g} is average energy gap and n_{v} the effective density of valence electrons [S17]. Thus, the electrostatic coefficient τ is determined by the energy gap and effective density of valence electrons and bounded by a limit to its dielectric constant-independent prefactor. At zero frequency, metals behave like perfect conductors with infinite permittivity, under which the electrostatic coefficient τ is also bounded [e.g. the fractions in Eqs. (S33) and (S34) tends to unity for perfect conductors].

S3. LINE ELECTRON UPPER LIMIT TO QUANTUM INTERACTION STRENGTH

In this section, we derive the upper limit to g_{Q} for two-dimensional line electron beams, which assumes translational invariance along a transverse direction (relative to the electron velocity). Consider a line electron beam in the (x, z) plane and invariant in y. The charge density is assumed as $q = 1.6\times10^{-19}$ C/nm, which can be modified based on practical electron beam properties. The frequency-dependent current density can be written as $\mathbf{J}(\mathbf{r},\omega) = -q\delta(z-z_0)\,\mathrm{e}^{\mathrm{i}\omega x/v}\hat{\mathbf{x}}$, where q is the charge density per unit transverse length. The incident electric fields and the magnetic fields in the frequency domain are obtained as follows. In the $z > z_0$ region

$$\begin{cases} \mathbf{E}_{\mathrm{inc}}(\mathbf{r},\omega) = \dfrac{q}{2\omega\epsilon_0}\mathrm{e}^{\mathrm{i}\omega x/v-\kappa_\rho(z-z_0)}\left(\dfrac{\omega}{v}\hat{\mathbf{z}} - \mathrm{i}\kappa_\rho\hat{\mathbf{x}}\right), & \text{(S36a)} \\ \mathbf{H}_{\mathrm{inc}}(\mathbf{r},\omega) = -\dfrac{q}{2}\mathrm{e}^{\mathrm{i}\omega x/v-\kappa_\rho(z-z_0)}\hat{\mathbf{y}}; & \text{(S36b)} \end{cases}$$

in the $z < z_0$ region

$$\begin{cases} \mathbf{E}_{\mathrm{inc}}(\mathbf{r},\omega) = -\dfrac{q}{2\omega\epsilon_0}\mathrm{e}^{\mathrm{i}\omega x/v+\kappa_\rho(z-z_0)}\left(\dfrac{\omega}{v}\hat{\mathbf{z}} + \mathrm{i}\kappa_\rho\hat{\mathbf{x}}\right), & \text{(S37a)} \\ \mathbf{H}_{\mathrm{inc}}(\mathbf{r},\omega) = \dfrac{q}{2}\mathrm{e}^{\mathrm{i}\omega x/v+\kappa_\rho(z-z_0)}\hat{\mathbf{y}}. & \text{(S37b)} \end{cases}$$

Here, $\kappa_\rho = \sqrt{(\omega/v)^2-(\omega/c)^2}$ and $v = \beta c$ is the velocity of electrons.

For such a 2D case, the volume integral element $\mathrm{d}V$ in Eq. (5) in the main text reduces to a rectangular area integral element $\mathrm{d}S$ with length L. By substituting Eq. (S37a) into the general limit Eq. (5) in the main text, we obtain the line-electron limit

$$\begin{aligned} |g_{\mathrm{Q}}|^2_{\mathrm{2D}} &\le \frac{\pi q^2}{16\hbar\epsilon_0}\frac{\tau}{\omega_0}\left(k_{v,0}^2+\kappa_{\rho,0}^2\right)\Theta(\omega;\omega_0,\Delta\omega)\int_S \mathrm{e}^{-2\kappa_{\rho,0}|z-z_0|}\,\mathrm{d}S \\ &\le \frac{\pi q^2}{16\hbar\epsilon_0}\frac{\tau}{\omega_0}\left(k_{v,0}^2+\kappa_{\rho,0}^2\right)\int_S \mathrm{e}^{-2\kappa_{\rho,0}|z-z_0|}\,\mathrm{d}S \\ &= \frac{\pi q^2}{32\hbar\epsilon_0}\frac{\tau\left(k_{v,0}^2+\kappa_{\rho,0}^2\right)L}{\omega_0\kappa_{\rho,0}}\mathrm{e}^{-2\kappa_{\rho,0}d}, \end{aligned} \tag{S38}$$

where $\kappa_{\rho,0} = \sqrt{k_v^2-k_0^2}$, $k_{v,0} = \omega_0/v$, $k_0 = \omega_0/c$, ω_0 is the target photon frequency, and d is the distance between the electron line beam and the scatterer.

S4. POINT ELECTRON SHAPE-INDEPENDENT UPPER LIMIT TO QUANTUM INTERACTION STRENGTH

In the cylindrical coordinate (x, ρ, ψ), the frequency-dependent incident field generated by the free electron with current density $\mathbf{J}(\mathbf{r},\omega) = -\frac{e}{2\pi\rho}\mathrm{e}^{\mathrm{i}\omega x/v}\delta(\rho)\hat{\mathbf{x}}$ can be expressed as [S8]

$$\mathbf{E}_{\mathrm{inc}}(\mathbf{r},\omega) = \frac{e\kappa_\rho\mathrm{e}^{\mathrm{i}\omega x/v}}{2\pi\omega\epsilon_0}\left[\mathrm{i}\kappa_\rho K_0(\kappa_\rho\rho)\hat{\mathbf{x}} - \frac{\omega}{v}K_1(\kappa_\rho\rho)\hat{\boldsymbol{\rho}}\right], \tag{S39}$$

where K_{n} is the modified Bessel function of the second kind. Combing Eq. (5) in the main text and Eq. (S39) we can rewrite the general limit equation

$$\begin{aligned} |g_{\mathrm{Q}}|^2_{\mathrm{3D}} &\le \frac{\pi\epsilon_0\tau}{4\hbar}\Theta(\omega;\omega_0,\Delta\omega)\omega_0\int_V |\mathbf{E}_{\mathrm{inc}}(\omega_0)|^2\,\mathrm{d}V \\ &\le \frac{\pi\epsilon_0\tau}{4\hbar}\omega_0\int_V |\mathbf{E}_{\mathrm{inc}}(\omega_0)|^2\,\mathrm{d}V, \end{aligned} \tag{S40}$$

where

$$\int_V |\mathbf{E}_{\mathrm{inc}}(\omega_0)|^2\,\mathrm{d}V = \frac{\alpha\hbar c}{\pi\epsilon_0\omega_0^2}\iiint\left[\kappa_{\rho,0}^4K_0^2(\kappa_{\rho,0}\rho)+\kappa_\rho^2k_{v,0}^2K_1^2(\kappa_{\rho,0}\rho)\right]\rho\mathrm{d}\rho\mathrm{d}\psi\mathrm{d}x, \tag{S41}$$

in which α is the fine-structure constant. When a free electron travels above a scatterer with a minimum separation d, one can use a concentric sector with height L, radius $\rho \in [d, \infty)$ and opening azimuthal angle $\psi \in (0, 2\pi]$ that encloses the scatterer to derive the bound analytically. Therefore, Eq. (S39) can be further simplified into a shape-independent limit given by

$$\begin{aligned}
\int_V |\mathbf{E}_{\mathrm{inc}}(\omega_0)|^2 \mathrm{d}V &\leq \frac{\alpha\hbar c}{\pi\epsilon_0\omega_0^2} L\psi \int_{\kappa_{\rho,0}d}^{\infty} \kappa_{\rho,0}\rho \left[\kappa_{\rho,0}^2 K_0^2(\kappa_{\rho,0}\rho) + k_{v,0}^2 K_1^2(\kappa_{\rho,0}\rho)\right] \mathrm{d}(\kappa_{\rho,0}\rho) \\
&= \frac{\alpha\hbar c}{\pi\epsilon_0\omega_0^2} L\psi \frac{(\kappa_{\rho,0}d)^2}{2} \left\{\kappa_{\rho,0}^2 \left[K_1^2(\kappa_{\rho,0}d) - K_0^2(\kappa_{\rho,0}d)\right] + k_{v,0}^2 \left[K_0(\kappa_{\rho,0}d)K_2(\kappa_{\rho,0}d) - K_1^2(\kappa_{\rho,0}d)\right]\right\} \\
&= \frac{\alpha\hbar c}{\pi\epsilon_0\omega_0^2} L\psi \left\{\kappa_{\rho,0} d k_{v,0}^2 K_0(\kappa_{\rho,0}d)K_1(\kappa_{\rho,0}d) - \frac{(\kappa_{\rho,0}d)^2}{2} k_0^2 \left[K_1^2(\kappa_{\rho,0}d) - K_0^2(\kappa_{\rho,0}d)\right]\right\} \\
&\leq \frac{\alpha\hbar c}{\pi\epsilon_0\omega_0^2} L\psi k_{v,0}^2 \kappa_{\rho,0} d K_0(\kappa_{\rho,0}d)K_1(\kappa_{\rho,0}d),
\end{aligned} \tag{S42}$$

where we use the relations $\int xK_{\mathrm{n}}^2(x)\,\mathrm{d}x = \left[K_{\mathrm{n}}^2(x) - K_{\mathrm{n}-1}(x)K_{\mathrm{n}+1}(x)\right]x^2/2$, $K_{-1}(x) = K_1(x)$, $K_2(x) - K_0(x) = 2K_1(x)/x$ and $K_1(x) > K_0(x)$ [S18].

Combining Eqs. (S40) and (S42) yields a general point-electron shape-independent limit of g_{Q} [Eq. (7) in the main text].

S5. PHOTON ENERGY CUTOFF OF LINE-ELECTRON LIMIT

The frequency cutoff condition Eq. (8) corresponds to a zero of the second-order derivative of the 2D limit Eq. (6) in logarithmic scale:

$$\begin{aligned}
\frac{\partial^2\left(|g_{\mathrm{Q}}|_{\mathrm{2D}}^2\right)}{\partial(\log\hbar\omega_0)^2} &\propto \frac{\partial^2\left[\left(k_{v,0}^2 + \kappa_{\rho,0}^2\right)\mathrm{e}^{-2\kappa_{\rho,0}d}/\omega_0\kappa_{\rho,0}\right]}{\partial(\log\hbar\omega_0)^2} \\
&\propto \omega_0 \frac{\partial}{\partial\omega_0}\left\{\omega_0 \frac{\partial\left[\left(k_{v,0}^2 + \kappa_{\rho,0}^2\right)\mathrm{e}^{-2\kappa_{\rho,0}d}/\omega_0\kappa_{\rho,0}\right]}{\partial\omega_0}\right\} \\
&= \omega_0 \frac{\partial}{\partial\omega_0}\left[\frac{2d\omega_0\left(v^2 - 2c^2\right)\mathrm{e}^{-2\kappa_{\rho,0}d}}{c^2v^2}\right] \\
&= \frac{2d\omega_0\left(2c^2 - v^2\right)\left(2\kappa_{\rho,0}d - 1\right)\mathrm{e}^{-2\kappa_{\rho,0}d}}{c^2v^2} \\
&= 0.
\end{aligned} \tag{S43}$$

Solving Eq. (S43) and discarding the zero-frequency solution, we have $2\kappa_{\rho,0}d = 1$, which is the cutoff condition of the line-electron upper limit.

S6. POINT-ELECTRON LIMIT DISCUSSION

A. Optimal photon energy at given electron energy

The optimal electron- and photon-energy condition of Eq. (9) corresponds to a zero of the first-order derivative of the point-electron limit $|g_{\mathrm{Q}}|_{\mathrm{3D}}^2$ Eq. (7) with respect to photon energy $\hbar\omega_0$:

$$\begin{aligned}
\frac{\partial(|g_{\mathrm{Q}}|_{\mathrm{3D}}^2)}{\partial(\hbar\omega_0)} &\propto \frac{\partial\left[\omega_0\kappa_{\rho,0}dK_0(\kappa_{\rho,0}d)K_1(\kappa_{\rho,0}d)/\beta^2\right]}{\partial\omega_0} \\
&\propto d\omega_0^2\left(v^2 - c^2\right)\left[K_0^2(\kappa_{\rho,0}d) + 2K_1^2(\kappa_{\rho,0}d) + K_0(\kappa_{\rho,0}d)K_2(\kappa_{\rho,0}d)\right] + 4c^2v^2\kappa_{\rho,0}K_1(\kappa_{\rho,0}d) \\
&\propto K_0(\kappa_{\rho,0}d)K_1(\kappa_{\rho,0}d) - \kappa_{\rho,0}d\left[K_0^2(\kappa_{\rho,0}d) + K_1^2(\kappa_{\rho,0}d)\right] = 0,
\end{aligned} \tag{S44}$$

where $K_0'(x) = -K_1(x)$, $2K_1'(x) = -K_0(x) - K_2(x)$ are used in the derivation [S18]. The last row of Eq. (S44) produces the optimal condition Eq. (9) of $|g_Q|^2_{3D}$ in the main text.

B. Optimal electron energy at given photon energy

The optimal electron energy for a given separation and photon energy can be alternatively obtained by a zero of the first-order derivative of Eq. (7) with respect to the electron energy $\mathcal{E}_0$:

$$\begin{aligned}\frac{\partial(|g_Q|^2_{3D})}{\partial\mathcal{E}_0} &= \frac{\partial v}{\partial\mathcal{E}_0}\frac{\partial(|g_Q|^2_{3D})}{\partial v} \propto \frac{\partial v}{\partial\mathcal{E}_0}\frac{\partial\left[\frac{\omega_0}{c\beta^2}\kappa_{\rho,0}dK_0(\kappa_{\rho,0}d)K_1(\kappa_{\rho,0}d)\right]}{\partial v}\\ &\propto k_{v,0}^2 d\left[K_0^2(\kappa_{\rho,0}d) + K_1^2(\kappa_{\rho,0}d)\right] - 2\kappa_{\rho,0}K_0(\kappa_{\rho,0}d)K_1(\kappa_{\rho,0}d)\\ &\propto \frac{\gamma^2}{2}\kappa_{\rho,0}d\left[K_0^2(\kappa_{\rho,0}d) + K_1^2(\kappa_{\rho,0}d)\right] - K_0(\kappa_{\rho,0}d)K_1(\kappa_{\rho,0}d) = 0.\end{aligned} \tag{S45}$$

Unlike Eq. (10) that can be obtained from the transcendental equation of $z \equiv \kappa_{\rho,0}d$, an analogous simple condition cannot be obtained from the last row of Eq. (S45) because $\kappa_{\rho,0}d$ also implicitly depend on the Lorentz factor γ.

C. Origin of the fast-electron and slow-electron optimal regimes

We fix the separation distance and plot the point-electron upper limit $|g_Q|^2_{3D}$ Eq. (7) versus electron energy for various fixed photon energy, to show why there are two optimal regimes in Fig. 2c. As shown in Fig. S1a, the upper limit $|g_Q|^2_{3D}$ initially increases with electron energy, reaches a local maximum, decreases to a local minimum, and then slowly diverges. The fast-electron optimal regime in Fig. 2c stems from the $\ln(\gamma)$ divergence of the limit Eq. (7) in electron energy, as indicated by the divergence observed at high energies in Fig. S1a. On the other hand, the slow-electron optimal regime in Fig. 2c originates from the local maximum in Fig. S1a, which is, in fact, the solution to Eq. (S45).

D. Upper limit behaviors versus electron energies at typical photon energies

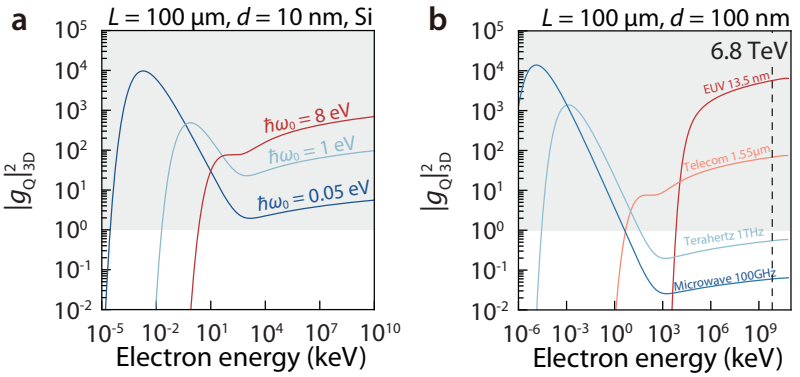

Figure S1. **Point-electron limit $|g_Q|^2_{3D}$ versus electron energy for different photon energy. a.** The upper limit $|g_Q|^2_{3D}$ of a Si half-plane, the interaction length L and separation distance d are set as 100 μm and 100 nm, respectively. **b.** The upper limit for typical materials and photon energies considered in Fig. 4. The black dashed line indicates 6.8 TeV electrons.

We provide more discussion on the trend observed in Fig. 4. We present the upper limit $|g_Q|^2_{3D}$ for a fixed interaction length $L = 100\,\mu$m and separation $d = 100$ nm for the four typical photon frequencies in Fig. 4, as shown in Fig. S1b. Indeed, even for low-energy photons at 1 THz and 100 GHz, if one continues to

increase the electron energy beyond 6.8 TeV, the upper limit of $|g_{\mathrm{Q}}|^2_{\mathrm{3D}}$ at can eventually exceed those at slow electron energies. This general behavior results from the $\ln(\gamma)$ logarithmic divergence of the upper limit $|g_{\mathrm{Q}}|^2_{\mathrm{3D}}$ as the electron energy tends to infinity.

Furthermore, for the considered configuration $L = 100\,\mu\mathrm{m}$ and $d = 100\,\mathrm{nm}$, 1 THz, 100 GHz and 1.55 μm photons satisfy the optimal condition Eq. (S45) of electron energy. This implies that $|g_{\mathrm{Q}}|^2_{\mathrm{3D}}$ initially reaches the slow-electron local maximum, then local minimum, as the electron energy increases before eventually diverging, which can be observed in Fig. S1b. Such behavior leads to the trend in Fig. 4c and d: $|g_{\mathrm{Q}}|^2_{\mathrm{3D}}$ decreases as β increases from 0.01 to 0.7 before hitting the local minimum and then diverges with increasing electron energy under considered separation. In contrast, 13.5 nm photon does not produce a zero solution to Eq. (S45) when $d = 100\,\mathrm{nm}$, resulting in a monotonic behavior of the upper limit $|g_{\mathrm{Q}}|^2_{\mathrm{3D}}$.

S7. ENERGY LOSS CALCULATIONS

A. Energy loss of point electron beam parallel to a half-space

We consider a point electron flying parallel to the surface of a 3D half-space with a constant velocity v along the x axis in the vacuum where relative permittivity $\epsilon_1 = 1$ (see the inset in Fig. 5b in the main text). The derivation has been reported in various literatures [S19; S20; S21; S22; S23], and here we provide a brief summary. The energy loss per unit length can be derived from the work done by the induced field on the electron:

$$-\frac{\mathrm{d}W}{\mathrm{d}x} = \mathrm{Re}\left[-eE_x^{\mathrm{ind}}\right], \tag{S46}$$

where W is the energy of the electron, E_x^{ind} is the x component of the induced electric field at the location of the electron. Here, E_x^{ind} corresponds to the scattered field in the $\mathbb{T}$-matrix framework; we use the induced-field notation to keep consistency with previous literature. The half-space with relative permittivity ϵ_2 is located at $z < 0$.

For an electron at $\mathbf{r} = (x, y, z)$ with the current in time domain $\mathbf{J}(\mathbf{r}, t) = -e\mathbf{v}\delta(\mathbf{R} - \mathbf{v}t)\delta(z - z_0)$ where $\mathbf{R} = (x, y, 0)$ represents its x-y projection, $\mathbf{v} = (v, 0, 0)$ and z_0 is the separation distance, the electric field in the frequency domain for $z < z_0$ can be written as [S23]

$$\mathbf{E}_0(\mathbf{K}, z, \omega) = \frac{\mathrm{i}4\pi^2 e}{4\pi\epsilon_0 k_z}\left(\frac{\omega}{c^2}\mathbf{v} - \mathbf{k}\right) \times \mathrm{e}^{-\mathrm{i}k_z(z-z_0)}\delta\left(\omega - \mathbf{K}\cdot\mathbf{v}\right), \tag{S47}$$

where $\mathbf{k} = (k_x, k_y, k_z)$ and $\mathbf{K} = (k_x, k_y, 0)$ are wavevectors, $k_z = \sqrt{\omega^2/c^2 - K^2}$, and the Fourier transforms are performed in time and $x - y$ space:

$$\mathbf{E}_0\left(\mathbf{K}, z, \omega\right) = \int \mathrm{d}R \int \mathrm{d}t\, \mathrm{e}^{-\mathrm{i}(\mathbf{K}\cdot\mathbf{R} - \omega t)}\mathbf{E}_0\left(\mathbf{R}, z, t\right). \tag{S48}$$

The incident field is a superposition of linearly polarized p− and s−polarized plane waves, and they are reflected by the surface with reflection coefficients r_{s} and r_{p}, respectively. The electric field at the surface ($z = 0$) which is tangential to the surface $\mathbf{E}^{z=0}_{\mathrm{p,tg}}$ is determined by

$$\mathbf{E}^{z=0}_{\mathrm{p,tg}} = -\frac{k_z}{K^2}E^{z=0}_{\mathrm{p}z}\mathbf{K}. \tag{S49}$$

With given r_{s} and r_{p}, the x component of the induced field at the surface sums up to

$$\begin{aligned} E_x^{z=0} &= E^{z=0}_{\mathrm{s}x} + E^{z=0}_{\mathrm{p}x} \\ &= \frac{k_y}{K^2}r_{\mathrm{s}}\left(E^{z=0}_{0x}k_y - E^{z=0}_{0y}k_x\right) - \frac{k_x k_z}{K^2}r_{\mathrm{p}}E^{z=0}_{0z} \\ &= r_{\mathrm{s}}E^{z=0}_{0x} - \frac{k_x k_z}{K^2}E^{z=0}_{0z}(r_{\mathrm{s}} + r_{\mathrm{p}}). \end{aligned} \tag{S50}$$

Here, $E_{\mathrm{sx}}^{z=0}$ and $E_{\mathrm{px}}^{z=0}$ denotes the s- and p-polarized induced electric field at the surface ($z = 0$),respectively. And $E_{0x}^{z=0}$, $E_{0y}^{z=0}$ and $E_{0z}^{z=0}$ are the x, y and z component of the incident electric field at the surface ($z = 0$), respectively. The time-domain real-space field is given by

$$E_x(\mathbf{R}, z, t) = \frac{\mathrm{e}^{\mathrm{i}k_z z}}{(2\pi)^3} \int \mathrm{d}K \int \mathrm{d}\omega \, e^{\mathrm{i}(\mathbf{K}\cdot\mathbf{R}-\omega t)} E_x^{z=0}(\mathbf{K}, 0, \omega). \tag{S51}$$

Recalling $\mathbf{x} = \mathbf{v}t$, combining Eqs. (S46), (S47), (S50), and (S51) produces the loss power

$$\begin{aligned} -\frac{\mathrm{d}W}{\mathrm{d}x} &= \mathrm{Re}\left[-eE_x^{\mathrm{ind}}\right] \\ &= \mathrm{Re}\left[-\frac{e\mathrm{e}^{-\mathrm{i}k_z z_0}}{(2\pi)^3} \int \mathrm{d}K \int \mathrm{d}\omega \, \mathrm{e}^{\mathrm{i}(\mathbf{K}\cdot\mathbf{R}-\omega t)} E_x^{z=0}(\mathbf{K}, 0, \omega)\right] \\ &= \frac{e^2}{2\pi^2\epsilon_0 v^2} \int_0^\infty \mathrm{d}k_y \int_0^\infty \omega \mathrm{d}\omega \, \mathrm{Re}\left\{-\mathrm{e}^{2\mathrm{i}k_z z_0}\left[\frac{k_z}{K^2}(r_{\mathrm{s}} + r_{\mathrm{p}}) + \frac{1}{k_z}\left(1 - \frac{v^2}{c^2}\right) r_{\mathrm{s}}\right]_{k_x=\omega/v}\right\}. \end{aligned} \tag{S52}$$

The total energy loss is an integration of the energy loss probability per unit frequency $\Gamma(\omega)$

$$-\frac{\mathrm{d}W}{\mathrm{d}x} = \int_0^\infty \hbar\omega \frac{\mathrm{d}\Gamma(\omega)}{\hbar \mathrm{d}x} \mathrm{d}(\hbar\omega). \tag{S53}$$

Thus, the energy loss in electron-volt per unit length is

$$\frac{\mathrm{d}\Gamma(\omega)}{\hbar \mathrm{d}x} = \frac{e^2}{2\pi^2\epsilon_0\hbar^2 v^2} \int_0^\infty \frac{\mathrm{d}k_y}{K^2} \mathrm{Re}\left\{k_z \mathrm{e}^{2\mathrm{i}k_z z_0}\left[\left(\frac{k_y v}{k_z c}\right)^2 r_{\mathrm{s}} - r_{\mathrm{p}}\right]\right\}. \tag{S54}$$

B. Energy loss of line electron beam parallel to a half-space

The energy loss of a line electron beam above a half space can be obtained by (1) defining the charge density q in the unit of Coulumb per unit length and (2) selecting the invariant momentum k_y (parallel to the surface and perpendicular to electron velocity). Note that we can choose a canonical 2D structure (like a half-space) to enclose a scatter such that k_y remains a conserved quantity. We are also free to choose the coordinate such that the line beam propagates along x and $k_y = 0$. We insert $2\pi\delta(k_y)$ into the integration of EELS Eq. (S54):

$$\frac{\mathrm{d}^2\Gamma}{\hbar \mathrm{d}x\mathrm{d}y} = \frac{q^2}{2\pi\epsilon_0\hbar^2 v^2} \int_{-\infty}^\infty \frac{\delta(k_y)\mathrm{d}k_y}{K^2} \mathrm{Re}\left\{k_z \mathrm{e}^{2\mathrm{i}k_z z_0}\left[\left(\frac{k_y v}{k_z c}\right)^2 r_{\mathrm{s}} - r_{\mathrm{p}}\right]\right\}, \tag{S55}$$

which can be simplified into

$$\frac{\mathrm{d}^2\Gamma(\omega)}{\hbar \mathrm{d}x\mathrm{d}y} = \frac{q^2}{2\pi\epsilon_0\hbar^2\omega^2} \kappa_z \mathrm{e}^{-2\kappa_z z_0} \mathrm{Im}\{-r_{\mathrm{p}}\}, \tag{S56}$$

where $\kappa_z = -\mathrm{i}k_z$ is a real wavevector.

C. Energy loss of point electrons passing close to a sphere

The energy loss of a point electron beam passing near a sphere under aloof excitation can be derived based on the Mie theory [S8; S24]. The total energy loss of the electron along the trajectory is given by

$$\Gamma(\omega) = \frac{e^2}{4\pi\epsilon_0 c\hbar\omega} \sum_{l=1}^\infty \sum_{m=-l}^{l} K_m^2 \left[\frac{\omega(a+d)}{v\gamma}\right] \left[C_{lm}^M \mathrm{Im}\{t_l^M\} + C_{lm}^E \mathrm{Im}\{t_l^E\}\right], \tag{S57}$$

where a is the radius of the sphere, d is the separation distance between the electron and sphere, γ is the Lorentz factor, and K_m is the modified Bessel function of order m. C_{lm}^M and C_{lm}^E stand for the electron-sphere coupling coefficients, and t_l^M and t_l^E are the magnetic and electric Mie scattering coefficients, which are given by

$$C_{lm}^M = \frac{1}{l(l+1)} |2mN_{lm}|^2, \tag{S58}$$

$$C_{lm}^E = \frac{1}{l(l+1)} \left| \frac{c}{v\gamma} M_{lm} \right|^2, \tag{S59}$$

with

$$N_{lm} = \sqrt{\frac{(2l+1)}{\pi} \frac{(l-|m|)!}{(l+|m|)!}} \frac{(2|m|-1)!!}{(v\gamma/c)^{|m|}} C_{l-|m|}^{(|m|+1/2)} \left(\frac{c}{v}\right), \tag{S60}$$

$$M_{lm} = N_{lm+1} \sqrt{(l+m+1)(l-m)} + N_{lm-1} \sqrt{(l-m+1)(l+m)}, \tag{S61}$$

and

$$t_l^M = \frac{-j_l(x_1)x_2 j_l'(x_2) + x_1 j_l'(x_1) j_l(x_2)}{h_l^{(+)}(x_1)x_2 j_l'(x_2) - x_1 \left[h_l^{(+)}(x_1)\right]' j_l(x_2)}, \tag{S62}$$

$$t_l^E = \frac{-\epsilon_1 j_l(x_1) \left[x_2 j_l(x_2)\right]' + \epsilon_2 \left[x_1 j_l(x_1)\right]' j_l(x_2)}{\epsilon_1 h_l^{(+)}(x_1) \left[x_2 j_l(x_2)\right]' - \epsilon_2 \left[x_1 h_l^{(+)}(x_1)\right]' j_l(x_2)}, \tag{S63}$$

where ϵ_1 and ϵ_2 are the relative permittivities of background and the sphere, l is the order of associated Legendre polynomials (also known as the multipolar order of the excitation, and $l = 1$ for dipple excitation), $C_m^{(v)}$ is Gegenbauer polynomial, $x_1 = \omega a \sqrt{\epsilon_1}/c$,$x_2 = \omega a \sqrt{\epsilon_2}/c$, primed functions denote their derivatives, and j_l and $h_l^{(+)} = \mathrm{i} j_l - y_l$ stand for spherical Bessel and Hankel functions, respectively.

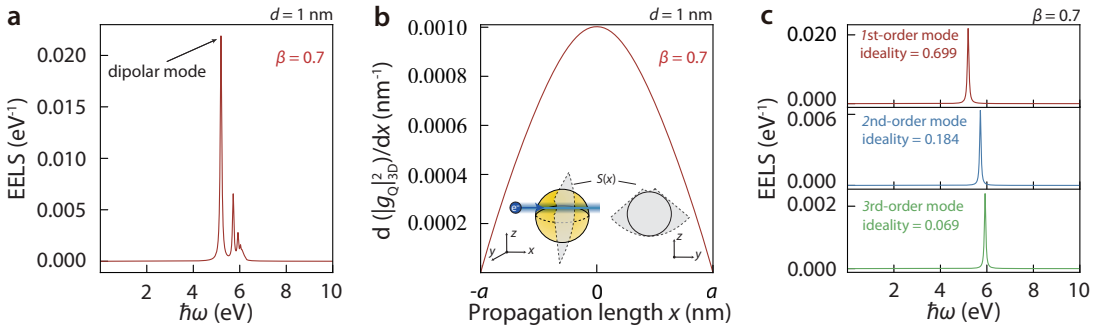

Figure S2. **Upper limit for an isolated sphere. a.** Energy loss spectra of the sphere. A point electron with velocity $\beta = 0.7$ interacts with a 3D isolated sphere made of Drude metal [$\epsilon_\mathrm{m} = 1 - \omega_\mathrm{p}^2/\omega(\omega + \mathrm{i}\gamma_\mathrm{m})$, $\omega_\mathrm{p} = 9.06\,\mathrm{eV}$, $\gamma_\mathrm{m} = 0.071\,\mathrm{eV}$ for gold]. The sphere has a radius of $a = 5\,\mathrm{nm}$, and the nearest separation between the electron and the sphere is $d = 1\,\mathrm{nm}$ **b.** Calculation details containing the upper limit $|g_\mathrm{Q}|_\mathrm{3D}^2$ per unit propagation length above the sphere. The inset shows the annular sector integral element $S(x)$ enclosing the circular cross-section of the sphere. **c.** Modal decomposition of electron energy loss near the sphere. We consider the same scenario as in Fig. S2a and show the decomposed spectra for the lowest three modes of Fig. S2a.

Fig. S2a shows the energy loss spectrum for the isolated sphere with $d = 1\,\mathrm{nm}$ and electron velocity $\beta = 0.7$ according to Eq. (S57). The highest peak at the lowest frequency indicates the excitation of the dipole mode ($l = 1$), while other peaks correspond to the excitation of higher-order modes. In the calculation of the theoretical bound for the sphere (solid lines in Fig. 5a), we integrate the incident field in the following manner: We consider the volume as $V = \int_{-a}^{a} S(x)\,\mathrm{d}x$, where $S(x)$ is the area of a minimal annular sector of enclosing the circles of the sphere at each x (see inset of Fig. S2b). Based on this scheme, the variable per-length upper limit of $|g_\mathrm{Q}|^2$ for $\beta = 0.7$ and $d = 1\,\mathrm{nm}$ is shown in Fig. S2b, whose x-integration yields the $|g_\mathrm{Q}|^2$ limit without defining a propagating length.

We further demonstrate the modal decomposition of the energy loss spectrum of the sphere by using the modal coefficients obtained from Eq. (S57). Fig. S2c shows the energy loss from the first to the third

order and their associated ideality. The ideality corresponding to the nth-order mode is computed from the spectral integration of a single angular momentum channel $l = 1, 2, 3, \cdots$ divided by the integral of total energy loss (that is, the integral of the energy loss in Fig. S2a).

S8. VALIDATION OF LINE-ELECTRON UPPER LIMIT

In this section, we present the validation of the derived line electron upper limit Eq. (6) by considering the line electron passes above a Drude-metal half-space in vacuum and excites surface plasmon polaritons (SPPs) at frequency ω_{SPP}. Same as the point electron for half-space case in main text, such scenario permits analytical treatment of energy loss Eq. (S56) to validate the line-electron upper limit Eq. (6). As depicted in Fig. S3, the analytical results closely follow the line electron upper limit Fig. S3 at the given separation d.

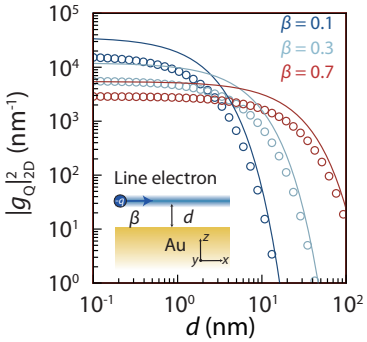

Figure S3. Comparison between the analytical calculation and the theoretical line electron upper limit. A line electron with charge density $q = 1.6 \times 10^{-19}$ C/nm interacting with a half-space made of a Drude metal [$\epsilon_{\mathrm{m}} = 1 - \omega_{\mathrm{p}}^2/\omega(\omega + \mathrm{i}\gamma_{\mathrm{m}})$, $\omega_{\mathrm{p}} = 9.06\,\mathrm{eV}$, $\gamma_{\mathrm{m}} = 0.071\,\mathrm{eV}$ for gold]. The interaction length is fixed at 100 µm.

S9. INTEGRATION INTERVAL CHOICE FOR INTERACTIONS STRENGTH AND IDEALITY

A. Sphere

In Fig. 5a, we compute $|g_{\mathrm{Q}}|^2$ when electrons excite the dipole mode of a sphere. The integration of energy loss of the sphere is considered over two full-width-half-maximum (FWHM) from $(\mathrm{Re}\,\omega_0 - 2\,\mathrm{Im}\,\omega_0)$ to $(\mathrm{Re}\,\omega_0 + 2\,\mathrm{Im}\,\omega_0)$ to cover the resonance such that we can isolate the resonance from the parasitic contribution of the zero-loss peak when the electron is positioned in the far-field (see Sec. S11). Here, we utilize Mie theory to compute the complex resonant frequency ω_0 of the sphere. The optical properties of a sphere are defined by the eigenmodes, which manifest as poles of the scattering matrix coefficients in the plane of complex frequencies. One can calculate the scattering cross-section of the sphere in the complex frequency plane to extract the eigenfrequencies of the sphere. In Mie theory, the normalized cross-section of a spherical nanoparticle is given as [S25]:

$$\sigma_{\mathrm{SC}} = \frac{2c^2}{\omega^2 a^2} \sum_{l=1}^{\infty} (2l+1)(|a_l|^2 + |b_l|^2), \tag{S64}$$

with

$$a_l = \frac{n\psi_l(nx)\psi_l'(x) - \psi_l(x)\psi_l'(nx)}{n\psi_l(nx)\xi_l'(x) - \xi_l(x)\psi_l'(nx)}, b_l = \frac{\psi_l(nx)\psi_l'(x) - n\psi_l(x)\psi_l'(nx)}{\psi_l(nx)\xi_l'(x) - n\xi_l(x)\psi_l'(nx)}, \tag{S65}$$

where $n = \sqrt{\epsilon_2/\epsilon_1}$ is the refractive index, ϵ_1 and ϵ_2 are the relative permittivities of background and the sphere, x is the size parameter defined as $x = \omega a/c$, $\psi_l(\rho) = \rho j_l(\rho)$ and $\xi_l(\rho) = \rho h_l^{(1)}(\rho)$. The eigenfrequencies ω_0 can be obtained by substituting complex frequencies ω into Eq. (S64), which corresponds to the singularities of the scattering cross-section σ_{SC} in the complex frequency plane [S26].

B. Half-space

In Fig. 5b and Fig. S3, we compute the $|g_{\mathrm{Q}}|^2$ of Drude-metal half-spaces when electrons excite SPPs at frequency ω_{SPP} . The permittivity of the Drude metal is defined as $\epsilon_{\mathrm{m}} = 1 - \omega_{\mathrm{p}}^2/\omega(\omega + \mathrm{i}\gamma_{\mathrm{m}})$, where ω_{p} is the plasma frequency and γ_{m} is the decay rate. Free electrons in vacuum can excite SPPs with wavevector $k_{\mathrm{SPP}} = \frac{\omega}{c}\sqrt{\frac{\epsilon_{\mathrm{m}}}{\epsilon_{\mathrm{m}}+1}}$ when the phase-matching condition $\omega/v = k_{\mathrm{SPP}}$ is satisfied. The equation permits the derivation of the complex frequency of the excited surface plasmon ω_{SPP} with a constant imaginary part $\mathrm{Im}\,\omega_{\mathrm{SPP}} = -\gamma_{\mathrm{m}}/2$ regardless of the value of $\mathrm{Re}\,\omega_{\mathrm{SPP}}$. Therefore, the definite integral of the $|g_{\mathrm{Q}}|^2$ is calculated between $(\omega_{\mathrm{SPP}} - \gamma_{\mathrm{m}})$ and $(\omega_{\mathrm{SPP}} + \gamma_{\mathrm{m}})$ within an interval of two FWHMs (maintaining consistency with those in Sec. S9.A) such that the integration can adequately capture the spectral peak.

C. Integration window selection of numerical simulations

For numerical calculations where the complex eigenfrequencies are not readily available, the integral windows for $|g_{\mathrm{Q}}|^2$ and ideality have to be empirically truncated. In Fig. 5c-e, the integration window for $|g_{\mathrm{Q}}|^2$ is defined as the range between the two nearest local minima of energy loss below and above the desired mode.

For the ideality $I_m = |g_{\mathrm{Qu},m}|^2 / \sum_i |g_{\mathrm{Qu},i}|^2$ of the target mode m in Fig. 5f, the integration window for all modes in the denominator starts from the first local minimum between the zero-loss peak and the lowest-order mode and extends to high frequencies (typically a few tens of electronvolts) at which the optical energy loss has fully decayed.

D. Modal decomposition

To obtain a more rigorous ideality I_m of the mode of interest, one should perform Hermitian and non-Hermitian modal decompositions on the energy loss to separate the contributions of different modes.

In Hermitian systems, the mode expansion coefficient of the specific nth-order mode can be obtained by computing the inner product between the desired eigenmode $\psi_n(\omega)$ and the scattered field $\mathbf{E}_{\mathrm{scat}}(\omega) = \sum_n a_n(\omega)|\psi_n(\omega)\rangle$, which is given as $a_n(\omega) = \langle\psi_n(\omega)|\mathbf{E}_{\mathrm{scat}}(\omega)\rangle / \langle\psi_n(\omega)|\psi_n(\omega)\rangle$ [S27].

The ideality I_m of the mth-order mode can thus be defined as the ratio: $I_m = \frac{\int a_m(\omega)\mathrm{d}\omega}{\sum_{n=1}^{\infty}\int a_n(\omega)\mathrm{d}\omega}$.

In non-Hermitian systems, the modal expansion coefficients can also be defined but based on the quasi-normal mode theory [S28; S29], where the normalization and inner product both become unconjugated because of the biorthogonal characteristics of the non-Hermitian eigenstates. To illustrate this modal decomposition, we take the sphere case in S7.C as an example, and the electron energy loss and the corresponding ideality are shown in Fig. S2c.

S10. TIGHTNESS OF THE BOUND FOR TWO OPTIMAL DESIGNS

For small separation d, the Air-Al core-shell optimal design in Fig. 5e exhibits better tightness between the limit and the numerical results compared to the Air-GaP core-shell design in Fig. 5d. The Air-Gap and Air-Al core-shell designs behave differently because the latter better satisfies the single-mode condition at small d.

In the deviation of the general upper limit, we perform two inequalities: Firstly, we consider a designable region D encloses an arbitrary scatterer V, which gives us a sum-rule constraint $\mathbb{I}_V \leq \mathbb{I}_D$. Secondly, we apply the single-mode condition by setting $\mathbb{T}_i = \mathbb{I}_V$ for the resonant frequency. How close or far away from these two inequalities can be treated as a criterion for evaluating the tightness of the upper bounds.

For the Air-Al core-shell design, the 13 nm Al shell only allows the fundamental mode and forbids higher-order modes. The excitation of the fundamental mode is reflected by the single peak of the energy loss

spectrum at small d shown in Fig. S4b. Therefore, the Air-Al core-shell structure satisfies the single-mode condition, which results in tightness between the limit and the design at almost all separations.

In contrast, the larger shell thickness in the Air-Gap design supports multiple modes because of its larger cross-section. The excitation of multiple-order modes can be observed by two energy loss peaks in Fig. S4a. Consequently, the single-mode condition is not well satisfied at small separations, leading to reduced tightness of the upper limit in the separation range of $d \sim 1-10\,\text{nm}$ (see dashed line for $d = 5\,\text{nm}$ where two modes are excited). In contrast, for $d \approx 100\,\text{nm}$ (see the dashed line for 100 nm in Fig. S4a), the single-mode condition is better satisfied, leading to improve tightness of the limit in Fig. 5d at $d = 100\,\text{nm}$.

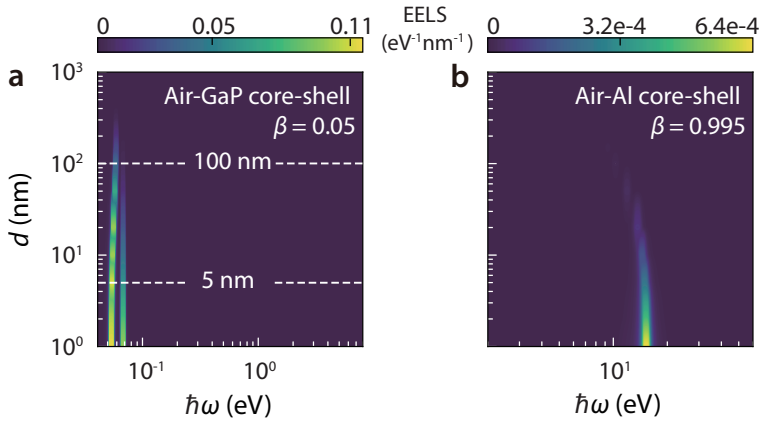

Figure S4. **Evolution of the energy loss spectra of the two near-optimal designs under various separations.** The single-mode condition is better satisfied in the Air-Al core-shell (**b**) than the Air-GaP core-shell structure (**a**).

S11. APPARENT BREAKDOWN OF THE LIMIT UNDER MULTIMODE CONDITIONS

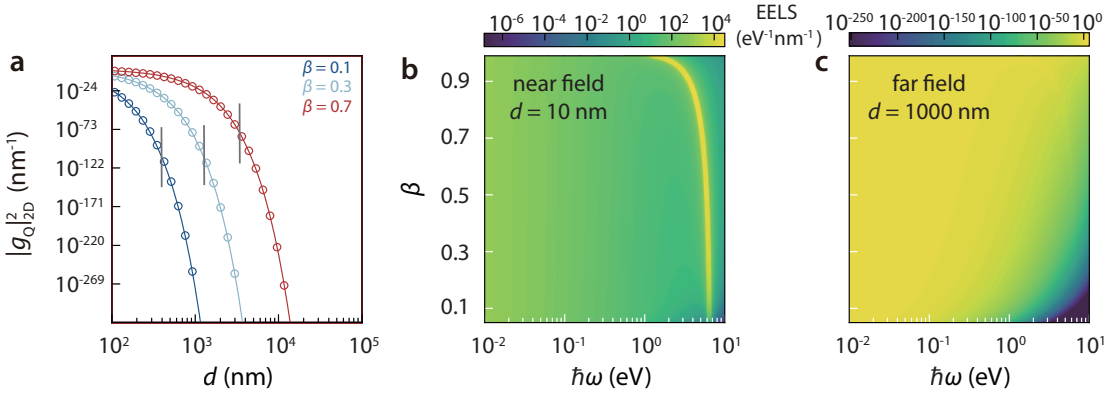

Figure S5. **Far-field breakdown of the line electron upper limit. a.** The limit can be broken for electrons in the far field when the separation d becomes larger than those indicated by the vertical black lines. Circles: numerical calculation of the 2D gold half-space; curves: the line-electron upper limit. The frequencies of the surface plasmons are near 6.39 eV, 6.26 eV and 5.27 eV for $\beta = 0.1$, 0.3, and 0.7, respectively. **b.** Energy loss of the line electron in the near field. The energy loss spectra exhibit clear peaks associated with SPPs excitation and satisfy the single-mode condition. **c.** Energy loss of the line electron in the far field. The SPPs peak reduces and gets immersed in the tail of the zero-loss peak, leading to the violation of the single-mode condition and the associated limit. The interaction length are fixed at 100 μm.

The derivation of the limits in this work relies on the single-mode condition, $\mathbb{T}_i = \mathbb{I}_V$ for the oscillator at ω_0. The condition can be violated when the spectral integration of energy loss no longer corresponds to

the $|g_Q|^2$ of the mode of interest, depending on the distribution of the eigenstates and source conditions. We provide an example using line electrons coupled with a half-space (Fig. S5).

In Fig. S5a, the energy loss exponentially decays as we extend the separation distance d between the line electron and the half space to the far field. The single-mode condition, valid in the near-field (Fig. S5b), no longer holds in the far-field (Fig. S5c), leading to the limits' breakdown when the separation d becomes larger than those indicated by the vertical black lines in Fig. S5a.

In the near field $d = 10\,\text{nm}$ (Fig. S5b), the energy loss manifests a clear peak originating from the coupling between the line electron and the SPPs modes at the phase-matching frequency ω_{SPP} (bright line in Fig. S5b). Thus, the single-mode condition for the derived limit is satisfied. As the line electron moves to the far field $d = 1000\,\text{nm}$ and larger separations, the SPPs loss peak reduces and eventually gets immersed into the zero-loss peak (Fig. S5c). As a result, the spectral integration of total energy loss at ω_{SPP} is predominated by the tail of the zero-loss peak, leading to the exceeding of the upper limit intended for the target SPPs mode at ω_{SPP}.

S12. EFFECTS OF MAGNETIC FIELDS

The main text of the paper deals with nonmagnetic materials. More generally, the effects of magnetic fields on $|g_Q|^2$ upper limits are relevant in two ways: (1) material responses to the "incident" magnetic fields generated by electrons; (2) the action of induced magnetic fields back onto electrons.

Material magnetic response: In the derivation of the upper limits, we assume nonmagnetic responses with relative permeability $\mu_r = 1$ that is typical at optical frequencies. As noted by the referee, this treatment should be generalized toward the microwave regime. To incorporate the effects of the material magnetic response in the upper limit of $|g_Q|^2$, one can consider the electromagnetic field $\mathbf{F}_{\text{inc}} = (\mathbf{E}_{\text{inc}}, \mathbf{H}_{\text{inc}})^{\text{T}}$ incident on a general medium with a 6×6 tensor material susceptibility $\overline{\overline{\chi}}$ containing both electric and magnetic parts and also modifying $\mathbb{T}$ matrix via Eq. (S14). It is thus interesting to derive the Kramers-Kronig and sum-rule relations for bianisotropic materials featuring simultaneous presences of electric and magnetic responses and their cross-coupling.

Back action of material magnetic response onto single electrons: For a single electron, the magnetic field of a photonic mode influences the radiation by coiling the electron's trajectory, resulting in a different $|g_Q|$, where $|g_Q|$ relates to the energy-loss integral along the trajectory. For the case of $|g_Q| \sim 1$, however, since the angular momentum of one photon is too small compared to that of a free electron, we can safely consider the electron trajectory as a straight line, unaffected by the spontaneous magnetic response from materials.

External magnetic fields: Microwave traveling wave tubes (TWTs) contain numerous external photons that can generate more pronounced magnetic fields to modify the electron trajectory. For simplicity, we consider an external magnetic field parallel to an electron beam. The resulting Lorentz force causes electrons to move in a helical path, which can help reduce the beam divergence in TWTs. The radius of curvature in the given point of the electron trajectory can be estimated by $R = \frac{v \sin\alpha}{(e/m_{\text{rel}})B}$ [S30], where α is the beam injection angle and $m_{\text{rel}} = m_0/\sqrt{1-\beta^2}$ is the relativistic electron mass, and m_0 is the rest mass. For an external magnetic field $0.1 - 1\,\text{T}$, the radius of helical motion is $0.1 - 1\,\mu\text{m}$ for electrons of energy $1 - 100\,\text{keV}$. Therefore, in this case, the helical motion of electrons should be considered for the (stimulated) quantum interaction strength.

S13. PRACTICAL LIMITATIONS TO MAXIMIZE INTERACTION STRENGTH

Practical limitations with slow electrons: The upper limits predict the enticing potential with slow electrons, but there also exist several technical challenges. First, it is challenging to observe photon exchanges with slow electrons at the state-of-the-art electron energy loss resolution. Second, when electron energy reduces, electron beam quality and collimation also deteriorate, posing practical issues in beam-sample alignment. Third, to couple with slow electrons, strong optical confinement is required. Graphene [S31] and plasmonic [S32] platforms could meet the need, but one also needs to mitigate the associated losses

for quantum applications.

Practical limitations with long structures and short gaps: Indeed, it is tempting to simply elongate the interaction length and shorten the interaction gap to increase the quantum interaction strength. However, this straightforward method also has practical limitations. First, in electron microscopes, unlike the idealized perfectly collimated point electrons, electron beams are focused on the sample plane and diffract afterward. Therefore, the interaction length (at desired small separations) cannot be arbitrarily increased at will; the effective propagation length is typically a few hundred micrometers in modern experiments. Second, the separation gap cannot be arbitrarily reduced either. Smaller gaps between electron beams and structures will cause excessive charge accumulation on the sample (especially dielectrics), which eventually repels the beam.

Taken together, practically (beyond the theoretical predictions here), it is a comprehensive task to select electron/photon energy and interaction length/gap to maximize $|g_Q|$ in experiments, where the optimal conditions may vary depending on various measurement conditions.

S14. DISCUSSIONS ON VARIOUS SPECTRAL REGIMES IN ACHIEVING STRONG INTERACTION

In Fig. 4, we discuss four technologically relevant frequency regimes with promising applications, namely EUV, telecommunication wavelength, terahertz, and microwave. Here, we comment on each spectral range to provide additional clarity and address the main challenges of each spectral regime for achieving $|g_Q|^2 > 1$.

- The emission of EUV (and even X-ray and γ-ray) photons has many important applications especially lithography and free-electron lasers. However, achieving $|g_Q|^2 > 1$ for EUV photons is already quite challenging for swift electrons $\beta \lesssim 0.7$ since it requires less than 10 nm separation for interaction length of hundreds of micrometer. Therefore, extreme relativistic electrons seem to be the only possible candidate.
- The visible-to-near-infrared regime (like the telecommunication wavelength in Fig. 4b) appears to be promising. Our upper limit does not rule out the possibility of $|g_Q|^2 \sim 10-100$ at almost all SEM and TEM energies for a feasible separation around 100 nm. Another advantage is the compatibility of this regime with integrated photonics and fiber-optic communications.
- The Terahertz and microwave regimes promise more prominent $|g_Q|^2$ at larger separations and could generate synergy with superconducting circuits. However, this advantage is at the cost of large device footprints and the lack of quantum optics interfaces.

REFERENCES

* Z. X. and Z. C. contributed equally to this work.
† owen.miller@yale.edu
‡ yiyg@hku.hk

[S1] V. Di Giulio, O. Kfir, C. Ropers, and F. J. García de Abajo, ACS Nano **15**, 7290 (2021).
[S2] O. Kfir, V. Di Giulio, F. J. García de Abajo, and C. Ropers, Science Advances **7**, eabf6380 (2021).
[S3] G. Huang, N. J. Engelsen, O. Kfir, C. Ropers, and T. J. Kippenberg, PRX Quantum **4**, 020351 (2023).
[S4] G. Baranes, S. Even-Haim, R. Ruimy, A. Gorlach, R. Dahan, A. A. Diringer, S. Hacohen-Gourgy, and I. Kaminer, Physical Review Research **5**, 043271 (2023).
[S5] H. T. Dung, L. Knöll, and D.-G. Welsch, Physical Review A **57**, 3931 (1998).
[S6] V. Di Giulio and F. J. García de Abajo, New Journal of Physics **22**, 103057 (2020).
[S7] V. Di Giulio, M. Kociak, and F. J. García de Abajo, Optica **6**, 1524 (2019).
[S8] F. J. García de Abajo, Reviews of Modern Physics **82**, 209 (2010).
[S9] P. Chao, B. Strekha, R. Kuate Defo, S. Molesky, and A. W. Rodriguez, Nature Reviews Physics **4**, 543 (2022).
[S10] S. Molesky, W. Jin, P. S. Venkataram, and A. W. Rodriguez, Physical Review Letters **123**, 257401 (2019).
[S11] L. Zhang, F. Monticone, and O. D. Miller, Nature Communications **14**, 7724 (2023).
[S12] R. Carminati and J. C. Schotland, *Principles of Scattering and Transport of Light* (Cambridge University Press, 2021).
[S13] O. D. Miller, Fundamental limits to near-field optical response, in *Advances in Near-Field Optics*, edited by R. Gordon (Springer International Publishing, Cham, 2023) pp. 25–85.

[S14] F. W. King, Journal of Mathematical Physics **17**, 1509 (1976).
[S15] H. Shim, L. Fan, S. G. Johnson, and O. D. Miller, Physical Review X **9**, 011043 (2019).
[S16] J. D. Jackson, Classical electrodynamics (1999).
[S17] S. Wemple and M. DiDomenico Jr, Physical Review B **3**, 1338 (1971).
[S18] M. Abramowitz and I. A. Stegun, *Handbook of mathematical functions with formulas, graphs, and mathematical tables*, Vol. 55 (US Government printing office, 1968).
[S19] A. Lucas and M. Šunjić, Physical Review Letters **26**, 229 (1971).
[S20] P. Echenique and J. Pendry, Journal of Physics C: Solid State Physics **8**, 2936 (1975).
[S21] A. Otto, physica status solidi (b) **22**, 401 (1967).
[S22] R. Garcia-Molina, A. Gras-Marti, A. Howie, and R. Ritchie, Journal of Physics C: Solid State Physics **18**, 5335 (1985).
[S23] F. Forstmann, A. Gras-Marti, T. Ferrell, R. Warmack, and K. Mamola, Physical Review B **44**, 4884 (1991).
[S24] F. J. García de Abajo and A. Howie, Physical Review Letters **80**, 5180 (1998).
[S25] C. F. Bohren and D. R. Huffman, *Absorption and scattering of light by small particles* (John Wiley & Sons, 2008).
[S26] S. Lepeshov, A. Vyshnevyy, and A. Krasnok, Nanophotonics **12**, 3729 (2023).
[S27] E. N. Economou, *Green's functions in quantum physics*, Vol. 7 (Springer Science & Business Media, 2006).
[S28] P. Lalanne, W. Yan, K. Vynck, C. Sauvan, and J.-P. Hugonin, Laser & Photonics Reviews **12**, 1700113 (2018).
[S29] W. Yan, R. Faggiani, and P. Lalanne, Physical Review B **97**, 205422 (2018).
[S30] S. E. Tsimring, *Electron beams and microwave vacuum electronics* (John Wiley & Sons, 2006).
[S31] F. H. Koppens, D. E. Chang, and F. J. García de Abajo, Nano Letters **11**, 3370 (2011).
[S32] Y. Adiv, H. Hu, S. Tsesses, R. Dahan, K. Wang, Y. Kurman, A. Gorlach, H. Chen, X. Lin, G. Bartal, *et al.*, Physical Review X **13**, 011002 (2023).